Journal of Power Sources 647 (2025) 237358

Contents lists available at ScienceDirect

Journal of Power Sources

journal homepage: www.elsevier.com/locate/jpowsour

Early detection of lithium plating during fast charging of lithium-ion batteries using nonlinear frequency response analysis

Julian Ulrich [a], Adrian Lindner [a], Tobias Brake [b], Martin Winter [b,c], Simon Wiemers-Meyer [b], André Weber [a], Ulrike Krewer [a,*]

[a] Karlsruhe Institute of Technology, Institute for Applied Materials – Electrochemical Technologies, Adenauerring 20b, 76131, Karlsruhe, Germany
[b] University of Münster, MEET Battery Research Center, Corrensstr. 46, 48149, Münster, Germany
[c] Helmholtz-Institute Münster, IMD-4, Forschungszentrum Jülich GmbH, Corrensstr. 46, 48149, Münster, Germany

HIGHLIGHTS

- Detection method for lithium plating using Nonlinear Frequency Response Analysis (NFRA).
- Significantly earlier detection of plating compared to known EIS-based methods.
- Model for inhomogeneous plating in a Newman-type cell model.
- Model-assisted understanding of the plating-related features in frequency response.

GRAPHICAL ABSTRACT

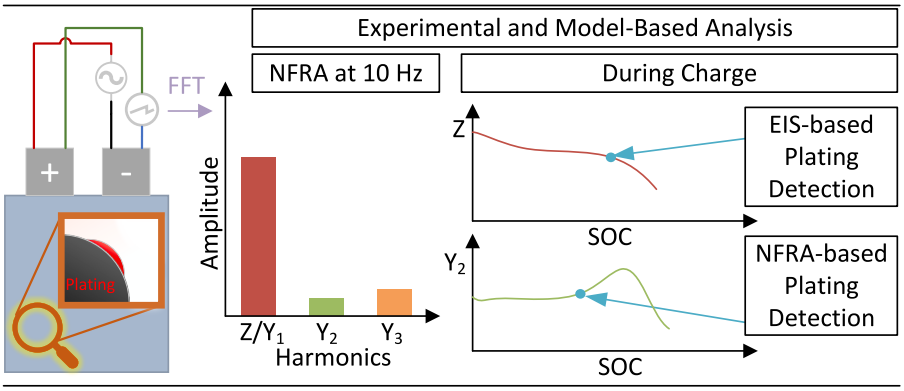

ARTICLE INFO

Keywords:
Degradation mechanisms
Lithium plating model
Intercalation stages
Nonlinear impedance spectroscopy
Safety

ABSTRACT

Safe fast charging of lithium-ion batteries is a central development goal of the automotive industry. This requires an early detection of lithium plating during the fast-charging procedure to avoid potentially hazardous dendrite formation.

In this paper, Nonlinear Frequency Response Analysis (NFRA) is shown to detect the occurrence of safety-critical lithium plating during the charging process earlier than Electrochemical Impedance Spectroscopy (EIS). NFRA measures higher harmonics, i.e., nonlinear behavior, in the cell's voltage response. This enables, compared to EIS, a more precise determination of the altered reaction kinetics due to plating.

For the first time, NFRA is applied during a charging process. When lithium plating occurs, the second harmonic first increases and later decreases with ongoing plating. This feature in the second harmonic is more pronounced and occurs significantly earlier than changes in the first harmonic considered by conventional EIS.

A cell model with plating reaction is applied to analyze the sensitivity of the NFR to plated lithium. Plating is modeled as an inhomogeneous layer only occurring on a part of the surface.

* Corresponding author.
E-mail address: ulrike.krewer@kit.edu (U. Krewer).

https://doi.org/10.1016/j.jpowsour.2025.237358
Received 26 March 2025; Received in revised form 26 April 2025; Accepted 10 May 2025
Available online 16 May 2025
0378-7753/© 2025 The Authors. Published by Elsevier B.V. This is an open access article under the CC BY license (http://creativecommons.org/licenses/by/4.0/).

The model reproduces the characteristic plating feature in the second harmonic as well as the experimentally observed decrease of impedance with state of charge. It thus enables a thorough interpretation of the dynamic cell behavior. Simulations show good agreement with experimental results, confirming that the second harmonic is more sensitive to plating than the impedance.

Thus, among all known electrochemical plating detection methods, analyzing the second harmonic can identify the onset of lithium plating earliest during fast charging.

1. Introduction

As lithium-ion batteries are one of the key energy technologies to attain a carbon neutral future, their safe and optimized usage is of high interest for both, society and industry. Especially fast charging constitutes an application, which pushes the technology to its limits of safe operation. This is mostly due to the undesired deposition of metallic lithium on the graphite anode of the cell, when high overpotentials form up at the active material surface [1–4]. Lithium plating can cause fast degradation and capacity loss. Growing dendrites of metallic lithium can even penetrate the separator and short-circuit the battery, leading to a thermal runaway event [1,5].

For safe, high-performance operation, an online detection method for the onset of plating is highly desirable. Plating significantly changes various properties of the electrochemical cell. Tracking changes in these properties leads to various detection methods for plating [2], including dilatometry [6–8], Nuclear Magnetic Resonance spectroscopy [9–11] and acoustic, supersonic-based methods [12].

Methods based only on the electrical response of the cell seem most appropriate for operando applications because of their cost effectiveness and wide applicability [2,13,14]. Here, two main paths have emerged. The first is based on the cell's behavior after a constant current charge: After deposition of lithium during charging, a distinct voltage plateau becomes visible in the relaxation phase, i.e. under open-circuit conditions [13,15,16]. The feature can be attributed to stripping of the metallic lithium. It is more prominent in the time derivative of the voltage. Based on the length of the plateau, the amount of plated lithium can be estimated. Therefore, this method can even be considered quantitative. Several studies analyze the voltage during the discharge directly after overcharge [13,15]. This has the advantage of not needing additional waiting time before discharging but is more error-prone [17]. Anyhow these methods are not able to detect plating during the charging phase and thus cannot be applied to detect the onset of the plating reaction and subsequently prevent further plating by an operando adaptation of the charging current profile.

The second path relies on the cell's dynamic response. Electrochemical Impedance Spectroscopy (EIS) was used to investigate the impact of the plating kinetics [13]. The polarization resistance determined from EIS was found to increase steadily and over a long period during the relaxation phase of a plated cell, whereas non-plated cells showed no such behavior. This is a strong indicator for faster kinetics of the plating/stripping reaction compared to the desired intercalation since EIS is expected to be sensitive to plating kinetics. Koleti et al. [18] were the first to make use of this behavior by tracking the polarization resistance during fast charging. They observed a distinct monotonous decrease of the impedance at a characteristic frequency after the onset of lithium plating. With higher charging rates, the decrease was observed earlier during charging, i.e. at lower states of charge (SOC). The behavior correlated well with the length of the voltage relaxation plateau. Therefore, this method is considered a powerful operando detection method for lithium plating. The results were successfully reproduced [19,20]. Katzer et al. [21] modified the approach by superposing the DC charging current with a small sinusoidal excitation to measure the cell's impedance at a characteristic frequency. Thereby, they got rid of additional waiting times during charging but were still able to obtain a similar decrease in impedance. The features were more visible, if first or second order derivatives of the impedance amplitude with respect to charge are used. In contrast, Brown et al. found an increase of cell impedance with the onset of lithium plating [22], which was not reproduced so far. A drawback of impedance-based plating detection is that a certain amount of plated Li is required before the impedance decrease can be observed. Furthermore, an additional decrease in impedance is introduced by the unavoidable increase of the battery temperature during fast charge, complicating the detection of Li-plating by EIS.

A different AC method for plating detection was presented in our previous study [23]. The study made use of so-called Nonlinear Frequency Response Analysis (NFRA) [24–28]. In NFRA (cf. Fig. 1 in SI), a much higher excitation amplitude than in EIS is used to stimulate nonlinear contributions in the cell's response. The amplitude of the second and third harmonic of the voltage response is then analyzed. Plating correlated with the amplitude of the third harmonic, Y_3, increasing faster than the second one, Y_2. The plating feature so far was only analyzed after several cycles where plating occurred.

Similarly, as in EIS, NFRA may also have potential for early and thus operando diagnosis. Followingly, in this study we combine the NFRA method with the charging protocol of Koleti et al. [18] to evaluate the potential of NFRA for early operando detection of plating and compare it to EIS. NFRA is especially sensitive to the charge transfer coefficients of the concerned electrochemical reactions [27–29], enabling improved identifiability of reaction kinetics in a P2D model [30]. Followingly, NFRA can not only detect changes in the reaction rate, but also in the

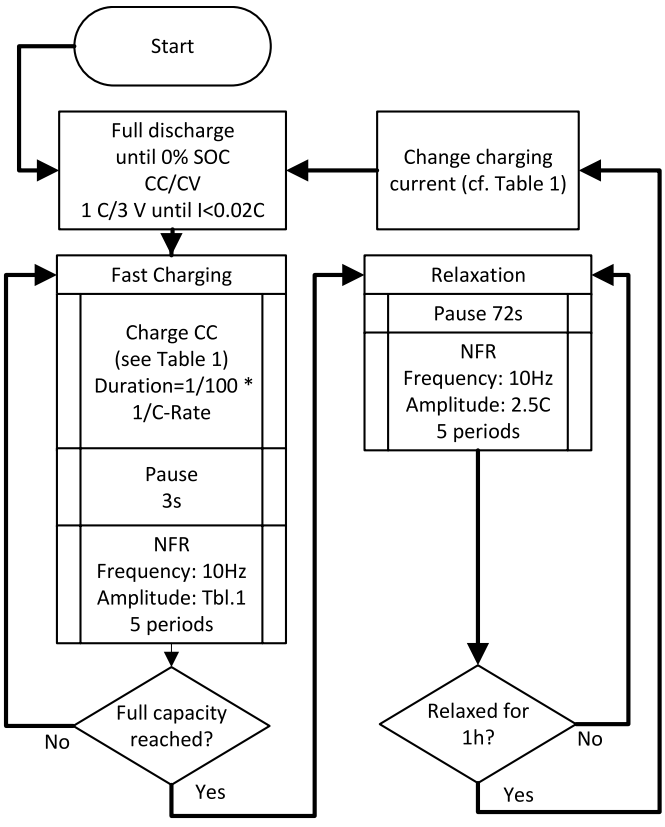

Fig. 1. Measurement procedure for plating detection.

ratio of oxidation and reduction current. This is, as shown in the results section, an important advantage over EIS.

NFR spectra are difficult to understand without physicochemical models. Basic models with Diffusion, Nernstian potential and Butler-Volmer kinetics show that solid diffusion excites both, the second and third harmonic, at low frequencies. In the medium frequency range, the charge transfer reactions are found, also exciting both harmonics, whereas changes in the charge transfer coefficient only impacts the second harmonic [28]. More complex interactions are seen for full battery models [31]. The NFR is significantly larger when a steady state is not yet reached [27].

In this study we present a new model for plating to interpret the results obtained from NFR measurements during a charging process with plating. Arora and White [3] were the first to introduce a plating model into a pseudo two-dimensional (P2D), Newman-type [32–34] cell model. In their work, as well as in subsequent approaches [10,35], the reaction happens homogeneously at the whole active surface area of the carbon electrode. The plating reaction begins when the anode potential falls below 0 V vs. a lithium reference. The amount of metallic lithium and therefore the thickness of the homogeneous layer is proportional to the integral of the plating current. The stripping reaction is mostly implemented with a condition that stops the stripping current if the amount of metallic lithium has reached zero. This often leads to discontinuous behavior of the simulation. Baker and Verbrugge [36] overcame this issue by introducing a surface concentration dependent activity of the metallic lithium. Therefore, a minute amount of metallic lithium, not enough for a monolayer, is always present in their model. Further stripping is kinetically hindered. Plating can happen before the anode potential reaches 0 V vs. Li/Li^+, which is also observed experimentally [37]. Hein et al. [38] used a similar approach to Ref. [36] for a 3D plating simulation on a microstructure. However, in contrast to Ref. [36], the film is not growing homogeneously on the whole active surface. Instead, for each surface element on the graphite particles, they introduced a growth mechanism, which first fills the area of the surface element with a monolayer and afterwards changes the layer thickness. The plating reaction only happens at the already partially covered surface elements. This inhomogeneous model is closer to reality, as seen from optical observations in Ref. [4]. So far, none of the models was used for NFR simulation.

In this study, we mainly use the formulation of Baker and Verbrugge [36] and introduce a new growth mechanism to obtain a partially covered electrode within a P2D model framework. It will be shown that changes in EIS and NFR during battery charge can be reproduced by the model. Additionally, the response is analyzed during relaxation. The model-assisted experimental analysis thus allows the correlation of linear and nonlinear responses with plating, leveraging the understanding of the frequency responses to facilitate the development of methods for early detection of plating.

2. Methods

2.1. NFRA definition

There are several definitions of how to conduct NFRA. We here follow a pragmatic approach of evaluating the amplitudes of the second and third harmonics as introduced in Harting et al. [25]; this contrasts with other groups who use frequency response functions, which easily become complex, and where therefore usually only the second harmonic is evaluated [24,39]. After a Fast Fourier Transformation of the voltage response to a large sinusoidal current excitation, nonlinearities emerge as measurable higher harmonics in the frequency domain (cf. Fig. 1 in SI). The amplitudes of the harmonics are displayed as a voltage and are named Y_k with the index k marking the response at k-times the excitation frequency. We adjust the inlet current amplitude I_0 such that the second harmonic Y_2 and the third harmonic Y_3 are well measurable, while harmonics of the order >3 do not exceed the noise level, which can also be identified by the potentiostat [40]. This avoids influence of higher order harmonics on the results of impedance, second and third harmonic, although the third harmonic may show a small impact on the measured apparent impedance [41]. In this study we do not measure EIS explicitly with low currents, therefore we always show the apparent impedance $Z = \frac{Y_1}{I_0}$, which may show minor deviations from an impedance measured with low current.

2.2. Experimental

2.2.1. Cell types

Tests on three different cell types were conducted. The main part of the study is on cell type 1, a 1 Ah commercial pouch cell from the manufacturer Li-FUN Technology with an NMC622 cathode and a graphite anode. To our best knowledge, there is no silicon used for the anode. The conducting salt is $LiPF_6$. The exact composition of the electrolyte remains unknown. Additionally, an experimental 0.17 Ah single-layered pouch cell (type 2) and a commercial 5 Ah 21700 cell (type 3) were investigated. Cell type 2 was manufactured by the Münster Electrochemical Energy Technology (MEET) research center. The cell is composed of an oversized graphite-based anode (121 mm × 68 mm) and a $LiNi_{0.6}Mn_{0.2}Co_{0.2}O_2$ (NMC622, 119 mm × 66 mm) cathode. The electrolyte consists of 1M $LiPF_6$ dissolved in EC:EMC (3:7 by weight). Cell type 3 is the INR21700-50E cylindrical cell from Samsung, consisting of an NCA cathode and a blend anode made from graphite and a small amount of silicon oxide. All cell types are listed in Table 1.

2.2.2. Setup and general characterization

For each cell type, the capacity was determined using a C/40 discharge from 4.2 V to 3 V. Additionally EIS was measured at 50 % SOC in a frequency range from 0.1 Hz to 10 kHz at all evaluated temperatures.

To set the ambient temperature for the cells, a Vötsch VT 4002 climate chamber was deployed.

For the electrochemical measurements, a ZenniumPro potentiostat from Zahner-Elektrik was used. Charging and discharging was performed using the Script function. For NFR measurements, which were started from the same script, the potentiostat was operated in NFRA mode (logfile entry = 6), which makes use of a special calibration routine developed by Zahner [40].

For the parameterization of cell type 1, an experimental EL-Cell PAT-Cell was built. One cell from cell type 1 was opened to extract electrodes for the experimental cell. This was possible since the electrodes were only coated single-sided at the end of the electrode wrap. The electrodes were washed in DMC and the cell was assembled with a glass fiber separator, a lithium reference and 150 µL of 1.0 M $LiPF_6$ in EC:DMC (1:1 by weight). After a 2 cycle C/10 formation, OCP for anode and cathode were obtained via a C/40 discharge with respect to the lithium reference ring. The voltage limits for the experimental cell were also 3 V and 4.2 V during formation and discharge.

2.2.3. Plating test procedure and conditions

The following measurement procedure (Fig. 1) for operando plating detection was inspired by the work of Koleti et al. [18]. The cell is discharged with 1C to 3.0 V at the given temperature and held at 3.0 V until the current falls below 0.02C. Afterwards, the cell is charged stepwise at a constant current, with the charge in a single step amounting to 1 % of the cell capacity. We set the maximum voltage to 4.6 V, which was never reached during the test, to allow for overcharge. This prevents discontinuities in the results due to a voltage limit and ensures that the transferred charge amount stays the same within each iteration, simplifying the analysis.

In contrast to the method from Koleti et al. [18], impedance is not measured using the voltage drop during relaxation. Instead, a sinusoidal excitation without DC part at a single frequency is used after the same

Table 1
Investigated cells with measurement parameters.

Type	Manufacturer	Format	Capacity	Investigated C-rates for Charging	NFRA Amplitude	Temp.
1	Li-FUN	Pouch	1 Ah	0.2C, 0.5C, 1C, 2C, 2.5C	2.5C	10 °C, 15 °C, 20 °C, 25 °C
2	MEET	Pouch	0.17 Ah	0.2C, 0.5C, 1C, 2C, 3C	5C	10 °C
3	Samsung	21700	4.9 Ah	0.1C, 0.2C, 0.5C	0.6C	5 °C

short relaxation time of 3 s at open-circuit conditions. The galvanostatic excitation uses such a high amplitude (see Table 1), that higher harmonics in the voltage response are well measurable and exceed the noise level. Due to the relatively high frequency in excitation, we do not expect significant contributions of the measurement current to plating, which was also not significant in simulations. However, this might be a point of investigation for future studies. It should be noted that the short relaxation time is not sufficient to obtain the time-invariant behavior required in conventional EIS and NFRA [31]. NFRA is conducted for five periods, while only the last four are used for the Fourier Analysis. The first wave of the response is discarded [40]. Short relaxation and measurement times are needed as reversibly plated lithium would intercalate in a longer relaxation period and thus would not be observable.

Additionally, the charging time would be unacceptably prolonged. Using just a single excitation frequency, the measurement time is kept short (0.5 s) and therefore enables the measurement of a quasi-steady state. The relaxation period was introduced to ensure the settling of charge transfer processes. We chose 10 Hz as excitation frequency, as this is a characteristic frequency where the response of the anode kinetics is observed [21], which was confirmed with analysis of the measured EIS spectra at 50 % SOC for all temperatures (c.f. section 11 in SI).

After each NFR measurement, we charged the cell with further CC steps, until the maximum capacity is reached. For a further insight into the behavior and changes of the potentially plated electrode after charging, we also measured the NFR fifty times during a 1-h relaxation period under open-circuit conditions. After the relaxation, the cell is discharged, and the charging experiment is conducted at the next higher charging current. In Fig. 9 of the SI, a fresh cell for each of the charging currents is used, confirming that the previous charging cycles do not significantly influence the measurement results. These cells were also opened to show the evolving surface film for the different C-Rates in Fig. 10 of the SI. The investigated C-rates during charge are given in Table 1.

For a full view on the potential of the method, we show the following analyses in this paper: First, the behavior of a single cell (type 1) is analyzed for varying charging current at 15 °C. Secondly, we also changed the ambient temperature to see the temperature effect on plating kinetics (c.f. Table 1). For each temperature a new cell was used, and the charging current was varied as in the first test. The first two studies were performed on cell type 1. Lastly, we also performed the measurement protocol with two other cell designs, i.e. cell type 2 and 3, to see if the trends in behavior are independent of cell design.

Due to restrictions of the potentiostat for the maximum current, we had to limit the maximum C-rate for cell type 3. Additionally, the excitation current for measuring the NFR of cell type 3 was limited to 0.6C. To induce significant lithium plating, the temperature was reduced to 5 °C. The lower capacity of cell type 2 results in the capability of increasing the excitation current for the NFRA measurements to achieve higher sensitivity towards lithium plating kinetics. Here, an excitation amplitude of 5C with a temperature of 10 °C were used to obtain significant lithium plating.

3. Modeling

3.1. Plating model

We used parts of the formulation of Baker and Verbrugge [36] as a starting point for the plating model and added inhomogeneous surface coverage of the plated metallic lithium. Yet, we neglected their theory of direct chemical intercalation of the deposited Li atoms into the graphite lattice since we are missing the experiments to parameterize chemical intercalation. The reintercalation process can be modeled sufficiently using just the electrochemical stripping with a subsequent intercalation step of the stripped lithium ions [3].

As in Ref. [36], small amounts of metallic lithium of less than a few monolayers thickness are assumed to interact with the electrode material. This lithium therefore does not show the activity of bulk metallic lithium. To model the transition of the Li activity from thickly plated Li ($\gamma_{Li} = 1$) to a negligibly plated electrode ($\gamma_{Li} = 0$), the activity coefficient for plated Li is modeled as

$$\gamma_{Li} = 1 - e^{-\frac{\Gamma}{\Gamma_{ref}}} \tag{1}$$

with the areal surface concentration Γ $\left(\frac{mol}{m^2}\right)$ and a reference surface concentration Γ_{ref}. This reference concentration is not clearly defined, but is usually selected in a range, which is equivalent to a few monolayer thick coating [36]. The value of this reference surface concentration mainly defines how sharp the transition is modeled. The corresponding open circuit potential (OCP) of the surface-influenced plated lithium vs Li/Li^+ will be zero for high surface concentrations $\Gamma \gg \Gamma_{ref}$, but – similarly to Li intercalation potential - above zero for low surface concentrations $\Gamma < \Gamma_{ref}$.

The current from the plating and stripping reaction is modeled as [36],

$$i_{pl} = i_{00,pl}\left(\frac{c_e}{c_{e,ini}}\right)^{1-\alpha_{pl}}\left(\left(1 - e^{-\frac{\Gamma}{\Gamma_{ref}}}\right)e^{\frac{(1-\alpha_{pl})F}{RT}(\Phi_s-\Phi_e)} - e^{\frac{-\alpha_{pl}F}{RT}(\Phi_s-\Phi_e)}\right) \tag{2}$$

with Φ_s, the electric potential in both graphite and Li solid, and Φ_e, the electric potential within the electrolyte. The latter is defined such, that it is given by the potential which an ideal Li/Li^+ reference would show at the evaluated point, as always in Newman-type models. The formulation transitions into an overpotential-based Butler-Volmer equation when $\Gamma \gg \Gamma_{ref}$. Once $\Gamma < \Gamma_{ref}$ is reached, the OCP equals that of graphite and stripping stops. Thus, minute amounts of metallic lithium are always present in the model. The anode potential depends on the interaction of the plating/stripping kinetics and intercalation kinetics.

Baker and Verbrugge [36] assumed a homogeneous film of metallic lithium on the graphite surface. Their homogeneous approach causes the simulated impedance to show only two inherent states: If no lithium deposit is present, the impedance is dominated by the intercalation reaction. Conversely, with metallic lithium, the impedance drops to a second value, where it is dominated by the faster exchange current density of the plating/stripping reaction. This behavior is contradictory to the observed continuous decline of the impedance during a fast charge [18,21].

To model the experimentally observed behavior, we treat plating inhomogeneously, which is closer to reality as seen in optical imaging [4]. The deposited lithium is not handled as a film with a constant thickness. Instead, we assume, that the deposited lithium consists of Li bodies growing on a fixed number of nuclei. These bodies of metallic lithium change their size during plating or stripping. They cover a certain specific area a_{pl} of the electrode. The concentration of metallic

lithium within the electrode can therefore be calculated using the specific area and the surface concentration Γ already known from Baker and Verbrugge [36],

$$c_{Li} = \Gamma a_{pl} \tag{3}$$

The change in concentration is given by the plating current using

$$\frac{dc_{Li}}{dt} = \frac{j_{pl}}{F} = \Gamma \frac{da_{pl}}{dt} + \frac{d\Gamma}{dt} a_{pl} \tag{4}$$

We assume a proportional growth of height and width of themetallic lithium bodies. The change of covered specific surface area is therefore directly linked to the surface concentration. The volume of one nucleus $V_{pl,nuc}$ divided by the surface it covers $A_{pl,nuc}$ on the anode is given by the molar volume of lithium $V_{m,Li}$ and the surface coverage Γ.

$$\frac{V_{pl,nuc}}{A_{pl,nuc}} = \underbrace{V_{m,Li}\Gamma}_{\lambda} \tag{5}$$

This is a characteristic length λ of the nucleus body, which may be referred to as its "thickness". The covered surface must be proportional to the square of this characteristic length. This is the nature of every three-dimensional body with constant proportions. Therefore, independently of the actual shape of the body of metallic lithium, the following relation holds:

$$a_{pl} = n_{nuc} \underbrace{k_{body} \lambda^2}_{A_{pl}} \tag{6}$$

The proportionality constant k_{body} describes the ratio of the electrode surface area, which is covered by one of the growing Li bodies to their squared characteristic "thickness" λ. The number of initial nuclei per volume n_{nuc} is assumed to be a constant. It relates the absolute surface covered by one body of metallic lithium to the volume specific surface of the electrode, which is covered by metallic lithium. This is a crucial homogenization step to describe surface coverage and concentration of metallic lithium in a continuous P2D model.

Inserting eq. (5) in eq. (6), the time derivative of the covered surface is therefore linked directly to the surface concentration of metallic lithium:

$$\frac{da_{pl}}{dt} = \underbrace{2 k_{body} n_{nuc} V_{m,Li}^2}_{k_{pl}} \Gamma \frac{d\Gamma}{dt} \tag{7}$$

For easier handling, we introduce k_{pl}, which depends on the proportionality constant, the volume specific number of nuclei and the molar volume of lithium. We named it "areal growth coefficient". Combining equations (4) and (7) yields the change in surface concentration:

$$\frac{d\Gamma}{dt} = \frac{j_{pl}}{F\left(a_{pl} + k_{pl}\Gamma^2\right)} \tag{8}$$

The surface covered by metallic lithium is then given by:

$$\frac{da_{pl}}{dt} = \frac{k_{pl}\Gamma j_{pl}}{F\left(a_{pl} + k_{pl}\Gamma^2\right)} \tag{9}$$

A central assumption in our model is, that intercalation only occurs at areas of the electrode not covered by plated Li, while plating only occurs in Li covered areas. Therefore, the volumetric current for plating and stripping is

$$j_{pl} = a_{pl} i_{pl} \tag{10}$$

and the intercalation current is given as

$$j_{int} = \left(a_s - a_{pl}\right) i_{int} \tag{11}$$

with a_s as the specific surface area of the porous electrode. This leads to the desired behavior that, with ongoing plating, the kinetics at the electrode transitions from pure intercalation towards pure plating kinetics. The total volumetric interfacial current is equal to the sum of the volumetric plating current, the volumetric intercalation current and the volumetric double-layer current.

All model equations can be found in the SI. The model was implemented in MATLAB 2024a. For a good numerical handling, some substitutions are necessary, which can also be found in section 7 of the SI.

3.2. Parameterization

A parameterization of the Li Plating extended P2D model was conducted only for cell type 1. The respective parameters are given in table 2. We did not aim to perfectly reproduce the cell behavior, but to find a parameter set, which is reasonable and good enough to analyze the frequency response of the cell during charging.

The model parameters can be divided into four parameter sets: Microstructural parameters, kinetic parameters, transport parameters and plating-related parameters. Microstructural parameters like particle size, porosity and tortuosity were obtained by microstructure reconstructions of X-Ray tomography and focused-ion beam - scanning electron microscopy scans of the anode and cathode respectively (see section 9 and 10 in SI). Kinetic parameters for the intercalation reactions were obtained by parameterizing the exchange current densities and double layer capacitances of both electrodes using an EIS measurement of the cell at 50 % SOC [42]. The charge transfer coefficient at the cathode was set to 0.47 to detect possible influences of the cathode on the results and not exactly to 0.5, which would suppress a second harmonic cathode response. The anode charge transfer coefficient was subsequently set to reproduce the second harmonic Y_2 at the beginning of a 0.2C charge (c.f. Figs. 2c and 8).

Activity coefficients of Li occupied or vacant sites within both anode and cathode material were determined based on the half-cell OCPs obtained from the experimental cell with reference. This measurement was also used to determine the internal cell balancing, respectively the maximum and initial Li-concentrations in the active materials. The transport parameters of the electrolyte are based on literature, while the solid diffusion coefficients were adapted to C-rate tests of the full cell [42].

Γ_{ref} was set to $10^{-5}\ \frac{mol}{m^2}$, a value which is low enough to provide a sharp transition between plating behavior and pure intercalation behavior. The value for the exchange current density of Li plating was gained from literature. While there is a vast variety [43] of values, we selected $10\ \frac{A}{m^2}$ from Ref. [3], as it is one order of magnitude higher than the exchange currents of the intercalation reactions. A charge transfer coefficient, $\alpha_{pl} = 0.3$ from Ref. [3], strongly overestimated the effect of plating on the second harmonic Y_2 (cf. Fig. 3 in SI). Therefore, 0.45 was chosen as it gave a reasonable progression of Y_2.

The areal growth coefficient is here assumed to be constant. It was set such, that the voltage relaxation profile after overcharging with 2C at 15 °C, becomes well visible and qualitatively reproduces the behavior from the measurements. The obtained value is $k_{pl} = 5 \times 10^3 \frac{m^3}{mol^2}$.

4. Results and discussion

4.1. Cell response for different charge currents

The pulsed charging procedure with NFRA in the charging breaks was conducted subsequently for five different currents. Fig. 2a shows the current and voltage progression. The maximum cell voltage during a full, dynamic charge is increasing with higher charging rates as overpotentials from charge transfer and charge transport are current-dependent (Fig. 2a). The corresponding absolute values of impedance and of the second and third harmonic are given vs. SOC during charge and vs. time during the relaxation period at 100 % SOC in Fig. 2b–d,

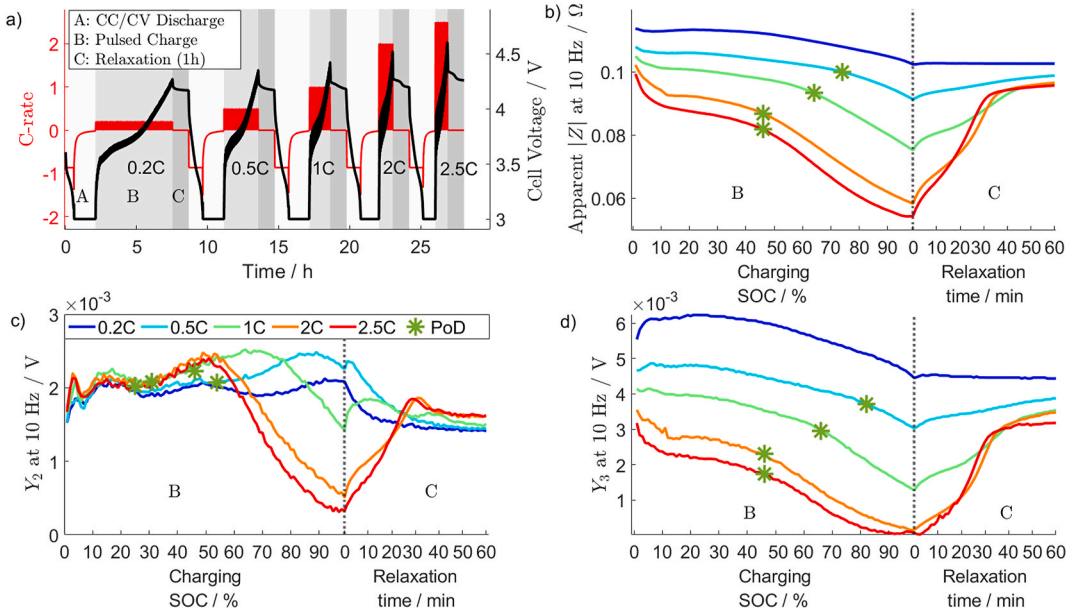

Fig. 2. Dynamic plating analysis of cell type 1 with different C-rates at 15 °C: (a) Cell voltage during discharge (A), charge (B) and relaxation (C) steps. Progression of the (b) apparent Impedance, (c) second harmonic Y_2 and (d) third harmonic Y_3 during charging, depending on the SOC (0–100) and during the 1 h relaxation period for an excitation of 2.5C. The green asterisks show the Points of Detection (PoD) for plating for each C-rate. PoD values for Y_2 have been determined from Fig. 4. (For interpretation of the references to colour in this figure legend, the reader is referred to the Web version of this article.)

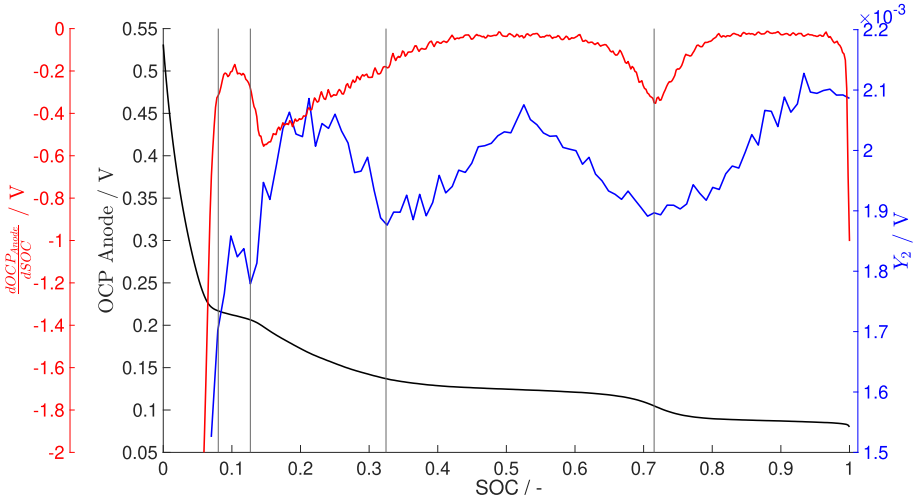

Fig. 3. Absolute value of the second harmonic, Y_2, open-circuit potential of anode and its gradient with respect to SOC during a 0.2C charge at 15 °C. The vertical lines mark characteristic points in the second harmonic.

respectively.

The higher charging rates of 1C and above lead to a pronounced voltage plateau in the voltage relaxation profiles (Fig. 2a, detailed in Fig. 2 in SI). The plateau can be considered as proof for the presence of metallic lithium [2,13]. From the relaxation profiles, we can conclude, that plating has happened in significant amounts at charging rates of 1C and higher, but small amounts may also be present at 0.5C. This was confirmed with the cell opening presented in Fig. 10 of the SI.

To analyze for indicators, when plating occurred during charge, we compare the progressions of the apparent impedance (Fig. 2b), as well as the nonlinear responses, i.e. the amplitude of the second harmonic Y_2 (Fig. 2c) and the third harmonic Y_3 (Fig. 2d) at the characteristic frequency of 10 Hz. For all three progressions, we marked the SOC as point-of-detection (PoD), which we interpret as the earliest indicator for lithium plating with the respective method. The points are added as a visual help to highlight kinks in the plots, which were determined using the second derivative of the signals (c.f. section 15 in SI). We determined by hand which of the available kinks is the one of interest.

For the impedance we expect a decrease of the response with the onset of lithium plating [18,21]. For 0.5C, this effect is visible from 74 % SOC, for 1C at approximately 64 % SOC and for 2C and 2.5C at approximately 46 % SOC. At 0.2C, a narrow range between 95 % and 100 % SOC also shows equivalent behavior. This suggests that even with minor current, there might be a slight deposition of Li, which was not visible within the voltage relaxation profile. The behavior of the impedance during relaxation is equally interesting to evaluate for plating impact, as the voltage relaxation had shown clear plating features. During relaxation, the impedance starts to increase again. For 0.2C, the impedance reaches a steady state within a couple of minutes, although the DC voltage is still relaxing. For higher charging currents, the impedance is monotonously increasing during relaxation. A steady state is reached after long relaxation times greater than 30 min. For

example, at 2C it takes approximately 40 min to reach a steady state. At 2 and 2.5C, the impedance shows an additional plateau similarly to the OCV. The duration of the monotonous increase clearly correlates with the length of the voltage plateaus in the voltage relaxation profile as seen in comparison with Fig. 2 in the SI. This suggests again that the decrease in impedance seen during charging is a measure for the degree of plating.

The higher harmonics Y_2 and Y_3 give additional insights on the reaction kinetics at the plated anode. Y_3 is known to be closely linked to the impedance response [27,28,31], since both voltage responses are odd harmonics. Therefore, assuming reaction kinetics as the main nonlinear process at 10 Hz, a change in impedance is also expected to lead to a similar change in the third harmonic. Indeed, this was observed in the measurements: The third harmonic decreases with impedance during lithium plating and increases again during reintercalation (Fig. 2d). The onset of the decrease in Y_3 is nearly equal to the onset of the decrease in the impedance. At 1C, the Y_3-decrease becomes visible between 60 % and 70 % SOC, just like for the impedance. Thus, for early detection of plating, Y_3 seems to have no advantages over the more easily measurable EIS.

The response of the second harmonic Y_2 contains additional information to the impedance. In the context of Butler-Volmer kinetics, Y_2 is a measure for the asymmetry between the oxidation and reduction branches of the polarization curve. This means, a charge transfer coefficient different from the value of 0.5 is the main cause for a high response in the second harmonic [24,28,29]. However, for values of the charge transfer coefficient different from 0.5, Y_2 will also decrease with the exchange current density [28]. Thus, Y_2 contains information on both, asymmetric kinetics and the exchange current density, which makes the analysis complex.

Up to a SOC of 30 %, Y_2 does not vary much with the applied charging current (Fig. 2c). Two distinct peaks can be seen within this range. In the measurement at 0.2C, there are two more additional maxima in Y_2 at SOCs over 30 %: One at approximately 50 % SOC and one close to 100 % SOC. When comparing the Y_2 profile at 0.2C with the open-circuit potential of the cell's anode (Fig. 3), the minima in Y_2 correspond well with transitions between different intercalation stages of graphite, which usually correspond to strong changes in the OCP with SOC.

This behavior is not yet fully understood. Reasons might be still ongoing equilibration processes from inhomogeneous charging of the cell or SOC dependent charge transfer coefficients for the intercalation reaction. So far, in literature there is to our best knowledge no focus laid on the SOC-dependence of the nonlinear reaction behavior.

Since we do not expect that plating happened in significant amounts during the 0.2C measurement, we conclude that the pronounced maxima and minima in Y_2 for 0.2C are mostly related to the intercalation process and not the plating reaction. As the behavior between 0 and 30 % SOC is identical also for higher C-rates, the same intercalation phenomena dominate Y_2 in this SOC range. In any case, this interesting correlation warrants further, more fundamental studies.

Significant deviations from the observed intercalation behavior in Y_2 at 0.2C are visible for higher charging rates and above ca. 50 % SOC. For 0.5C, Y_2 increases until 90 %, from where onwards it drops down. Thus, obviously, strongly different behavior is taking place for higher charging rates above 50 % SOC. For higher charging rates, Y_2 starts to increase even earlier but also decreases earlier. The decrease at high SOC is only observed at SOCs where EIS already shows the plating-related decrease. We attribute the behavior of Y_2 of an initial increase, reaching a maximum and subsequent decrease to the occurrence of lithium plating. The initial increase can be explained by a higher kinetic asymmetry, respectively a charge transfer coefficient with a stronger deviation from 0.5 of the plating and stripping reaction compared to the intercalation reaction. This deviation from 0.5 has been suggested in literature [3,44] based on model-based analysis of the discharge curves of previously overcharged cells. The transition in Y_2 thus results from the interaction of plating and intercalation kinetics, which could in combination lead to an overall apparent charge transfer coefficient, which deviates more and more from 0.5. Another reason for the increase in Y_2 might be the difference in OCP and thus in overpotentials for plating and intercalation, also resulting in an asymmetric behavior. However, in our model-based analysis this was not enough to generate the increase in Y_2 during plating (c.f. Fig. 3 in SI).

Further, as mentioned before, the second harmonic is also correlated to the exchange current density. Due to the plating-related increase in the overall apparent exchange current density, the second harmonic will start to decrease, just as the impedance, with ongoing plating. This interpretation is supported by the relaxation behavior: Only for 0.2C, i.e. the plating-free electrode, Y_2 decreases monotonously. All other C-rates show first an increase before a decrease sets in, which we explain as follows: During stripping, plated Li is removed and thus the overall exchange current density decreases to the level of the intercalation exchange current density. The increase in Y_2 is larger and longer the larger the charge current, i.e. the more the cell has been plated. Y_2 shows similarly to Y_3 and EIS an additional plateau >2C.

The maximum at the end of the increase of Y_2 clearly corresponds to the end of the plating-attributed plateau in the open circuit voltage (c.f. Fig. 2 in SI). The initial increase of Y_2 is more pronounced and happens earlier than the decrease in impedance, and the signal reaches a steady state also later than the impedance. This behavior suggests that the features in Y_2 are more sensitive towards plating than the already known plating-related feature of decrease in the impedance. Measuring Y_2 is thus a promising operando plating detection method. It may enable that the charging current could be restricted earlier, which makes fast charging safer and may enhance the battery life span.

The features from intercalation are not easily distinguishable from the plating-related features. To facilitate analysis, the difference of Y_2 to the plating-free Y_2 profile at 0.2C is displayed in Fig. 4. Having subtracted the features, that we attribute to SOC-dependent intercalation, only plating features are expected. Indeed, the increase and decrease of Y_2 due to plating is now better visible. We added the points, at which Y_2 increases, i.e. where we expect from our theory, that the onset of lithium plating happens.

4.2. Impact of temperature

It is known that plating of lithium-ion batteries heavily increases at low cell temperature [2]. Fig. 5 displays impedance and Y_2 during a 1C and 2C charge for climate chamber temperatures of 10 °C, 15 °C, 20 °C and 25 °C. The results of the impedance and the second harmonic are shown for charging currents of 1C and 2C in Fig. 5. The slower kinetics at lower temperatures should cause impedance and nonlinear frequency response in the respective frequency range to increase for decreasing temperature. On the other hand, plating has faster kinetics than intercalation. Thus, we also expect more and earlier plating and an earlier decrease in impedance for lower temperatures. These opposing trends indeed are visible in the responses. For low SOCs, where no or negligible plating is expected, impedance and Y_2 increase with lower temperature for both investigated C-rates. For 10 °C and 1C, both drop steeply around 40–50 % SOC, while the drop comes much later and slower for higher temperatures, leading to overall smaller impedance and Y_2 for 10 °C than for higher temperatures at 100 % SOC at 1C. We attribute this huge difference in dynamics to the much stronger prevalence of plating kinetics at 10 °C. Further, the second harmonic shows the expected increase of Y_2 with the onset of lithium plating for both evaluated C-rates. For 10 °C, this behavior is, as expected, more pronounced and detectable at lower SOC than for 15 °C. It is again well visible, that the increase in Y_2 happens earlier than the decrease in impedance. The point which defines the onset of plating shows a stronger change and thus is more pronounced than in the impedance feature. For higher temperatures, features in both become less distinct. At 20 °C, i.e. 5 °C above the standard temperature, lithium plating is still visible in both impedance

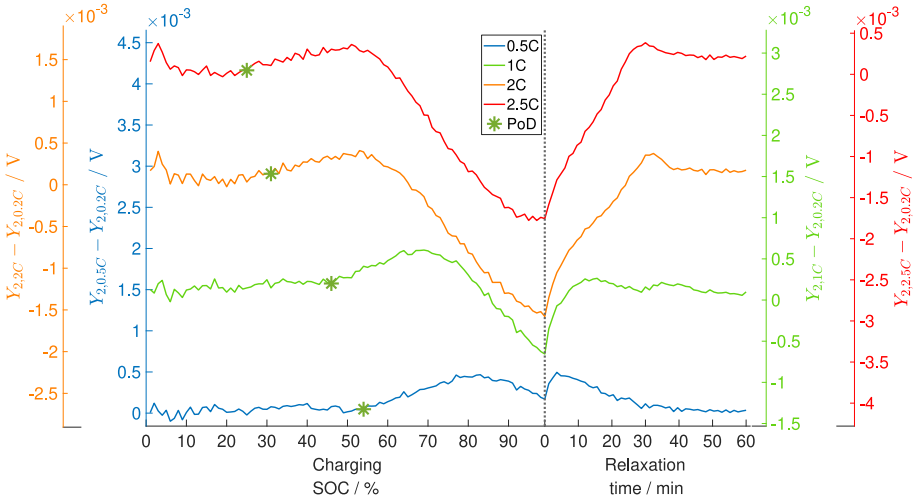

Fig. 4. Plating-feature in the Y_2 profile for cell type 1 at 15 °C: The profile at 0.2C was subtracted from the results for higher C-rates.

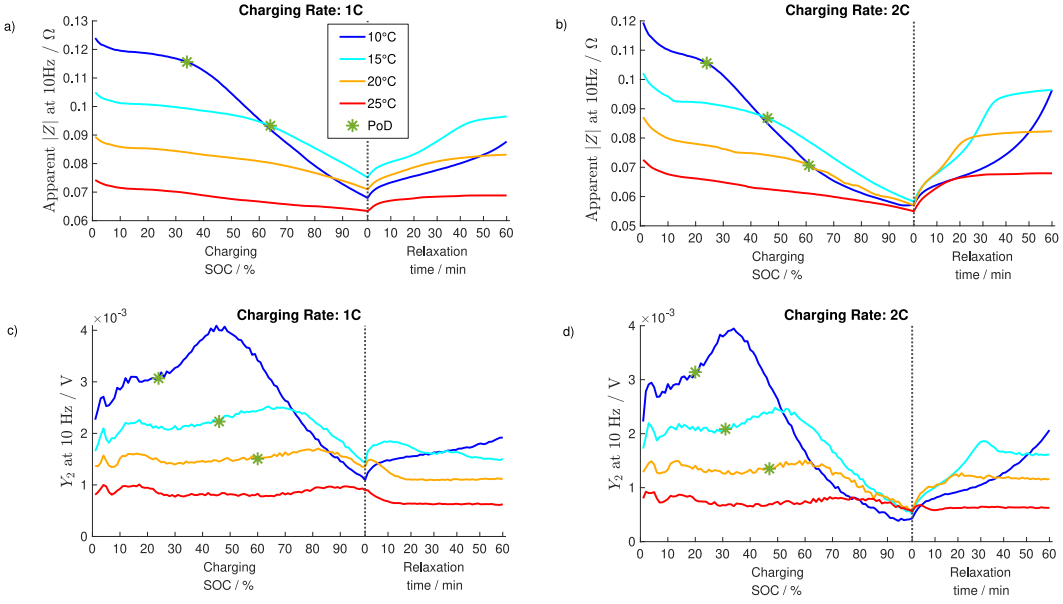

Fig. 5. Impact of temperature on impedance and Y_2 during charging and relaxation at open circuit: (a) Progression of the impedance for a charging rate of 1C and (b) for 2C charging. (c) Progression of Y_2 for 1C charging and (d) for 2C charging.

and Y_2. However, the distinction between plating features in impedance and Y_2 and the plating-free response from intercalation becomes harder. Finally at 25 °C and 1C, no plating features are visible.

All plating features are stronger for 2C, where also more plating and stripping is expected. At 15 °C and 2C, the increase in Y2 strongly overlaps with the intercalation feature at ~15 % SOC. Still a small change in slope is visible at 20 % SOC, where we added the PoD. For 2C and 25 °C, we can even find a small maximum in the start of the relaxation and an elongated increase of impedance during relaxation compared to 1C, which may indicate the presence of some metallic lithium. For 10 °C and both C-rates, the relaxation period of 1 h was not sufficient to reach a steady state.

In conclusion, the second harmonic response shows the expected dependency on temperature. The plating-related features are more pronounced for lower temperatures. However, the method is still applicable for different temperatures. Furthermore, in all cases, Y_2 allowed an earlier detection of plating than impedance.

4.3. Impact of cell design

Cell type 2 (c.f. Table 1) is a pouch cell similar to the previously analyzed cell type 1, yet with only one electrode layer and known composition. Cell type 2 was excited with a large (5C) current to get increased sensitivity in the harmonics. The temperature of cell type 2 compared to cell type 1 was changed from 15 °C to 10 °C to obtain sufficient lithium plating. With a temperature of 10 °C, lithium plating becomes detectable at currents of 2C and 3C, as displayed in Fig. 6a and c. During charging with a current of 2C and 3C the plating feature of a decreasing impedance is visible. Additionally, the second harmonic Y_2 shows an increase attributed to lithium plating. For lower C-rates, no clear inflection points in Y_2 were visible. Thus, we attributed the increase of the second harmonic for 0.5C and 1C to intercalation and added no PoD to the graph. For this cell, the feature for plating onset in Y_2 is even more distinct than for cell type 1, which is partly invoked by the higher excitation current. With a charging current of 1C, 2C and 3C, the second harmonic is having a maximum directly in the beginning of the relaxation period, accompanied by an initial decrease in impedance

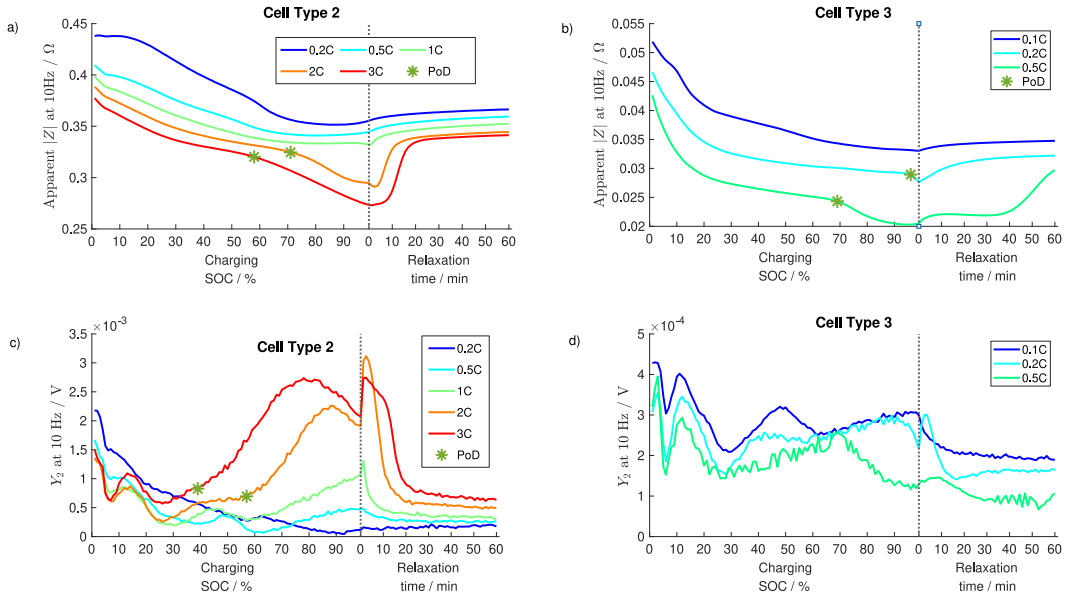

Fig. 6. Impact of cell type on progression of Impedance and Y_2 during pulse charging at various C-rates and relaxation. Excitation amplitude for cell type 2 was 5C and for cell type 3 0.6C (a) Impedance for cell type 2 at 10 °C and (c) corresponding Y_2. (b) Impedance for cell type 3 at 5 °C and (d) corresponding Y_2.

during relaxation. This is not yet fully understood and may be a side effect of the large excitation current.

Fig. 6b and d shows the results for cell type 3, a commercial 21700 cell with a nominal capacity of 4.9 Ah. It is the only cell type featuring some silicon in the anode, which may impact the NFR. The maximum excitation current of the potentiostat was already reached at 0.6C. To still get significant nonlinearities despite the low amplitude, the temperature was reduced to 5 °C. The measured second harmonic, however, is still one order of magnitude lower than for the other cells. The results are thus noisier in comparison. Still, the general behavior could be reproduced: The decrease in the impedance is well visible for 0.2C and 0.5C suggesting plating at these conditions. The increase in Y_2 is not distinguishable from the intercalation-related features, which dominate here in contrast to the other cells. However, the subsequent decrease in Y_2 is still well visible and corresponds to the impedance feature.

Within the relaxation period, Y_2 shows a maximum at 0.2C and 0.5C. This plating feature in Y_2 correlates well with the mentioned EIS plating feature for the same C-rates. We assume that a higher excitation current would be needed for this cell to get a more pronounced plating feature for Y_2 during charge.

The significantly different response for this cell may also be caused partly by Si as active material; distinguishing its effects would require though separate NFRA studies with cells with different Si content.

Summarizing the study on cell design, the identified plating features in EIS and Y_2 are also present in other cells with a graphite-based anode. The sensitivity can be tuned according to the cell by adapting the excitation current during NFR measurement.

4.4. *In-depth model-assisted analysis of plating features*

The identified plating features in Y_2 and impedance warrant a deeper analysis. This is conducted for the first time with a Li-Ion battery model with plating/stripping kinetics. Of special interest is to see whether the features are similarly visible at the onset of Li plating. The model was

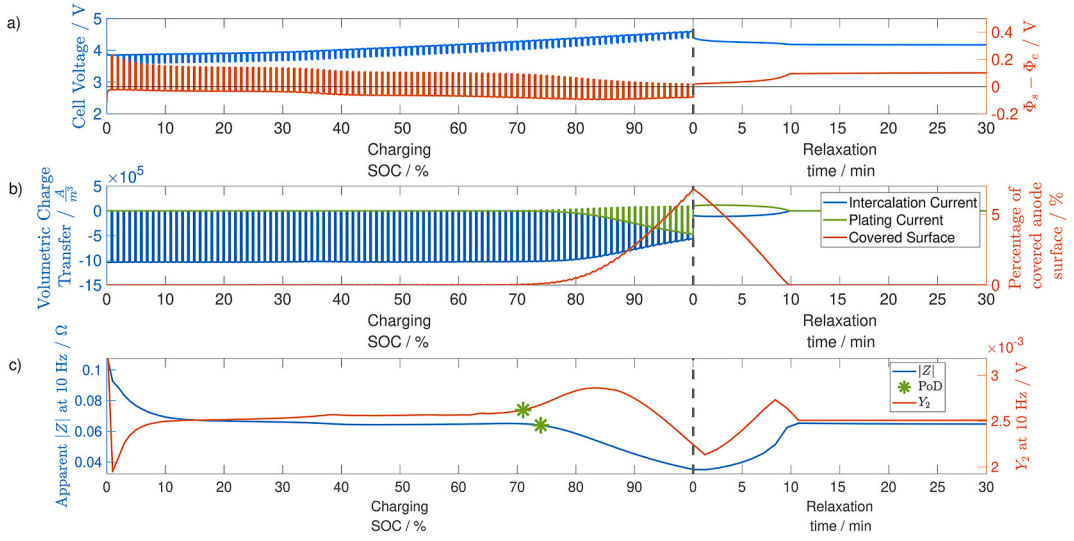

Fig. 7. Insights into the plating and stripping effects during simulation of a pulsed 3C charge at 15 °C with a subsequent relaxation period at OCV at 100 % SOC. NFR was simulated with 2.5C excitation. (a) Cell voltage and anode Galvani potential close to the separator. (b) Intercalation and plating current, as well as percentage of total electrode area covered by Li (c) Amplitude of impedance and second harmonic Y_2 progression depending on plating with points of detection for plating.

parameterized to cell type 1 and simulations follow the experimental protocol for charging, frequency measurements and relaxation time (c.f. Fig. 1). The NFR measurement is simulated in exactly the same manner as it is performed in experiment. The time-domain results containing the sinusoidal input and output are converted via FFT to frequency-domain while omitting the first wave, as it is done in the potentiostat.

Fig. 7 shows the results of a 3C pulsed charge simulation and the subsequent relaxation time. Similarly as in the experiments, cell voltage increases during the pulsed CC charge, with spikes occurring during the 3s relaxation time (Fig. 7a). As an indicator for the occurrence of plating, we also display the Galvani potential difference, $\Phi_s - \Phi_e$, between graphite and electrolyte at the separator. Plating takes place if this voltage falls below 0 V, since we define the potential difference equal to what would be measured between the anode and a Li/Li^+ reference, as it is common in Newman-type models.

Fig. 7b displays the area which is covered by metallic lithium with respect to the whole electrode surface at the interface to the separator. The separator interface is the first place in an electrode where plating would occur. In contrast to other models, where plated lithium always covers the whole surface of the electrode, here the covered area always stays below 5 % of the anode surface. It is visible, that plating does not occur in significant amounts directly after the Galvani potential falls below 0 V. This is the case because the charge pulses are followed by a break including a relaxation period and NFR, where stripping of metallic lithium can already happen. This is also shown in more detail in Fig. 7 of the SI. In fact, NFR can even mitigate the evolution of metallic lithium due to the asymmetry between plating and stripping reaction as shown in Fig. 8 of the SI. Once the break duration is not sufficient to reintercalate all plated Li, the surface concentration of metallic lithium increases strongly, as well as the Li coverage of the electrode. This comes with an increase of plating and decrease of intercalation current, as displayed in Fig. 7b. During relaxation, reintercalation takes place and intercalation and plating current have the same magnitude but opposite sign. Interestingly, the Galvani potential does not decrease monotonously during charge but rises again at a high SOC of approximately 85 %, as soon as Li covers more than ca. 1 % of the electrode surface. The underlying reason for the potential increase is that potential is more impacted by plating, and plating has faster kinetics and therefore less overpotential than intercalation. The increase in potential with plating is also known from measurements of the graphite potential vs. a lithium reference during charging [4]. Thus, our model can reproduce an important plating phenomenon. The growth of the surface film not only in thickness but also in area plays a crucial role in here.

During relaxation, the Galvani potential rises monotonously until it reaches the graphite open-circuit potential. This behavior is reflected in the full cell's open-circuit voltage, where the expected plating-related plateau is visible before reintercalation is completed. The time until a steady state is reached is directly linked to the lithium coverage, which is constantly reduced because of the ongoing stripping reaction. A detailed view of the simulated relaxation behavior and its C-rate dependence is available in the SI, Fig. 5.

Fig. 7c shows the simulated progressions of the apparent impedance and the second harmonic during charging and relaxation. As soon as there is a significant plating rate, i.e. at 72 % SOC, the impedance starts falling more steeply. This behavior is similar as in experiment (cf. Fig. 2). The simulation also reproduces the impedance increase during relaxation: Impedance increases until all metallic lithium is stripped. Simulation shows thus that the rapid impedance decrease during plating and increase during relaxation can be directly attributed to plating and stripping. Also, the plating feature in Y_2, i.e. the increase during plating can be reproduced by the model. In simulation too, this happens earlier than the decrease in impedance, confirming the higher sensitivity of Y_2 for plating detection. Two further features of Y_2 are well reproduced by the model: At high SOC, there is a maximum and Y_2 decreases again for plated cells; further, during relaxation Y_2 shows a maximum which is clearly correlated to plating. Also, Y_3 decreases with plating and increases during the 1-h relaxation phase as seen in Fig. 4 in the SI.

The progression of impedance and higher harmonics and plating-related features are thus qualitatively reproduced by the model, showing that the developed model is a sound representation of a Li-ion battery subjected to plating conditions. It thus gives insights and can provide explanation for the behavior observed in the measurements. The increased asymmetry, here introduced by the plating-related charge transfer coefficient showing values far from 0.5, is a necessary assumption to provide the desired results (cf. Fig. 3 in SI).

The model was not able to reproduce the wavy progression in the second harmonic correlating to the intercalation stages at low SOC. This shows that the P2D model is not yet capable to fully describe the nonlinear dynamics and the underlying complex intercalation kinetics. A possible explanation for the observed behavior might be, that the charge transfer coefficients are SOC dependent. This could for example be modeled with the so-called Multi-Species, Multi-Reaction [45,46]

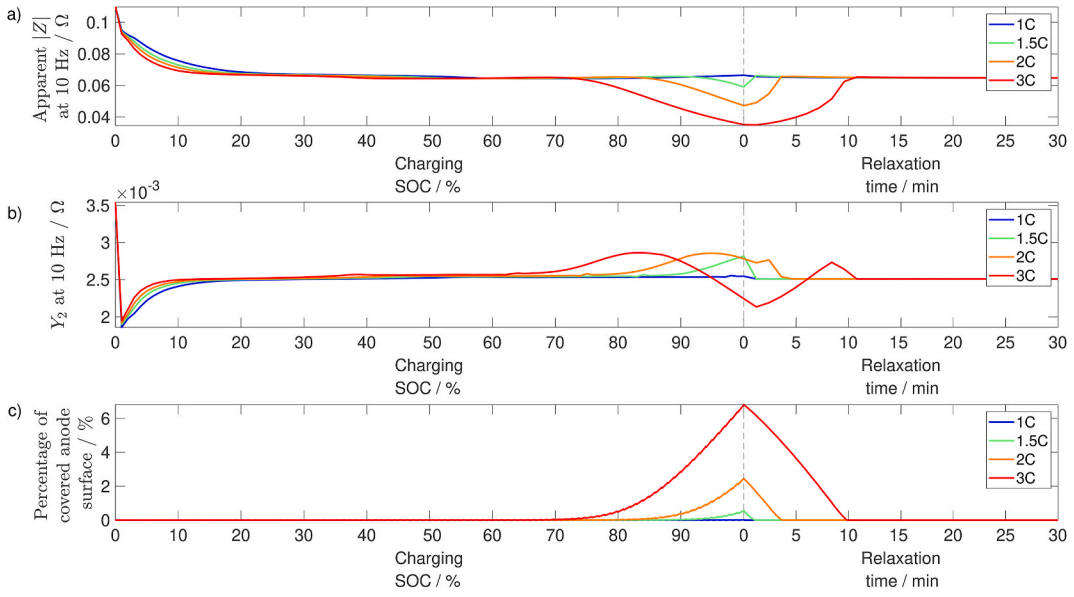

Fig. 8. Impact of charging current on the simulated frequency response during pulsed charging. (a) Impedance of the simulated cell (b) Second harmonic response Y_2 of the simulated cell (c) Coverage of anode with metallic lithium close to the separator in the simulated cell.

model, which assumes a separate reaction for each intercalation stage of graphite. These reactions could each be parameterized with a different charge transfer coefficient.

To check if the model can also describe the experimentally observed C-rate dependence during charge, the current was varied between 1 and 3C as seen in Fig. 8. For lower c-rates, plating starts at higher states of charge. This can be attributed to lower anode overpotentials for lower C-rates. During relaxation, impedance increases later for higher C-rates and more plating. Also, Y_2 increases later and less steep for charging at lower C-rates and Y_2 shows only a maximum during the relaxation phase for significantly plated electrodes. Importantly for plating detection, similarly as in experiment, in all cases Y_2 is more sensitive than impedance, as it shows the characteristic increase earlier, i.e. at lower SOC, than impedance. The PoDs are not shown here to provide better visibility of the progressions. The C-rate dependence of the harmonic responses clearly correlates, as in experiment, with the relaxation behavior under OCV conditions (see Fig. 5 in SI). The simulation confirms that the experimentally observed changes in frequency response indeed come from plating and that Y_2 is more sensitive to plating than impedance and thus an ideal candidate for early plating detection. Although the current parameterization of the model cannot reproduce the progressions of the harmonics and the onset of plating quantitatively, it is extremely useful to understand the interplay between plating and frequency response.

5. Conclusions

This work presented and explained the unique change of impedance and nonlinear frequency response behavior during plating and stripping and paves the way for unprecedentedly early plating detection during battery charging. It was found that not only the impedance, but also the second and third harmonic of the frequency response change heavily on the occurrence of lithium plating. Experimentally, we identified three features for the detection of lithium plating: The amplitude of the impedance and the third harmonic both decrease with the occurrence of lithium plating, which is attributed to the higher exchange current density of the plating reaction compared to intercalation. During relaxation at OCV after a full charge, stripping leads to an increase in impedance and third harmonic Y_3. The behavior of the impedance during charge and relaxation was for the first time simulated and well reproduced with our newly developed cell model with plating and stripping kinetics. This plating model was integrated in a P2D cell model, which allows studying the occurrence of plating and stripping in a battery, as well as to simulate frequency responses.

The third and most interesting feature can be found in the amplitude of the second harmonic Y_2. The second harmonic at first starts to increase with the onset of lithium plating and then decreases; during relaxation, again an overshoot in Y_2 is observed. This feature in Y_2 is strongly dependent on the charge transfer coefficient. The feature corresponds well to the features in impedance, third harmonic, voltage relaxation and to the found surface film after cell opening.

The theory on Y_2 was additionally confirmed with the plating model. The feature in the second harmonic shows a notably higher sensitivity to the onset of lithium plating than the features in impedance and the third harmonic. The higher sensitivity was demonstrated in both experiment and simulation. Therefore, the newly found feature is of very high interest for early operando plating detection during charging.

Future research may include further validation by applying other operando plating detection methods in parallel. Moreover, we encourage studies to transfer the here generated knowledge and method to practical application in devices. Options to shorten the measurement time include reducing the number of measurements or reducing the 3 s relaxation time. Furthermore, NFRA could be conducted with an overlayed DC current to fully avoid the additional waiting time introduced by our method. As a final step, a current controller based on the newly found plating feature could be developed, which could prevent lithium plating. This could be done by analyzing the derivative of the impedance and Y_2 features, as we have shown here. Alternatively, as a simpler and more practical approach, a threshold value for the increase of Y_2 could be used.

Moreover, our findings show research directions beyond the application to fast charging: Of high interest for fundamental understanding of graphite intercalation kinetics is the progression of the second harmonic during a slow charge. Distinct wave-like features at low SOC were discovered in Y_2. They were attributed to changes in intercalation kinetics and could not be reproduced by the models' one-step Butler-Volmer intercalation kinetics. Y_2 holds thus a unique opportunity also to study changes in intercalation kinetics due to internal material changes. Understanding this phenomenon, using advanced electrochemical models or first principle simulations could provide an even deeper insight into thermodynamics and kinetics of contemporary active materials. Additionally, a better discrimination of plating and intercalation effects may become possible.

The developed model also holds potential for future research: Further parameterization and model adaptions could allow a quantitative matching of simulation and experiment, which would enable to determine the amount of metallic lithium from purely electrochemical measurements. We also suggest the use of the here proposed area growth mechanism for cell and plating simulations. Our cell model could furthermore be extended to account for the frequency response at the solid electrolyte interphase (SEI). This would enable an even more detailed description of the measured data and could be crucial to quantify metallic lithium using frequency response.

CRediT authorship contribution statement

Julian Ulrich: Writing – original draft, Visualization, Validation, Software, Methodology, Investigation, Formal analysis, Data curation, Conceptualization. **Adrian Lindner:** Writing – review & editing, Validation, Methodology, Investigation. **Tobias Brake:** Writing – review & editing, Resources. **Martin Winter:** Supervision, Resources. **Simon Wiemers-Meyer:** Writing – review & editing, Supervision, Resources. **André Weber:** Writing – review & editing, Supervision, Resources, Funding acquisition. **Ulrike Krewer:** Writing – review & editing, Supervision, Resources, Funding acquisition.

Declaration of competing interest

The authors declare that they have no known competing financial interests or personal relationships that could have appeared to influence the work reported in this paper.

Acknowledgements

The authors acknowledge the financial support from the German Federal Ministry of Education and Research (BMBF) in the projects OSLiB (03XP0330B) within the competence cluster Battery Utilisation Concepts (BattNutzung) and the project MiCha (03XP0317B) within the competence cluster Analytics and Quality Assurance (AQua).

Appendix A. Supplementary data

Supplementary data to this article can be found online at https://doi.org/10.1016/j.jpowsour.2025.237358.

Appendix

4.5 Model Parameters

Table 2
Model Parameters

Parameter Name	Symbol	Value	Origin/Comment
P2D Parameter			
Anode thickness	d_a	$65 \times 10^{-6} m$	Measured with micrometer gauge
Cathode thickness	d_c	$70 \times 10^{-6} m$	Measured with micrometer gauge
Separator thickness	d_{sep}	$25.4 \times 10^{-6} m$	Measured with micrometer gauge
Anode porosity	ϵ_a	0.34	Microstructure reconstruction (see SI)
Cathode porosity	ϵ_c	0.34	Microstructure reconstruction (see SI)
Separator porosity	ϵ_{sep}	0.5	[47]
Anode tortuosity	τ_a	3.24	Microstructure reconstruction (see SI)
Cathode tortuosity	τ_c	2.19	Microstructure reconstruction (see SI)
Separator tortuosity	τ_{sep}	1.4	Bruggeman relation $\beta = 1.5$ [48]
Particle radius anode	R_a	$10 \times 10^{-6} m$	Microstructure reconstruction (see SI)
Particle radius cathode	R_c	$3.9 \times 10^{-6} m$	Microstructure reconstruction (see SI)
Solid diffusion coefficient anode	$D_{s,a}$	$1 \times 10^{-14} \frac{m^2}{s}$	Manual parameterization with C-rate test
Solid diffusion coefficient cathode	$D_{s,c}$	$0.5 \times 10^{-14} \frac{m^2}{s}$	Manual parameterization with C-rate test
Maximum solid concentration anode	$c_{s,max,a}$	$31833 \frac{mol}{m^3}$	[49]
Maximum solid concentration cathode	$c_{s,max,c}$	$51410 \frac{mol}{m^3}$	[49]
Initial solid concentration anode	$c_{s,ini,a}$	$20605 \frac{mol}{m^3}$	Adapted to C/40 quasi-OCV measurement
Initial solid concentration cathode	$c_{s,ini,c}$	$21500 \frac{mol}{m^3}$	Adapted to C/40 quasi-OCV measurement
Initial salt concentration	$c_{e,ini}$	$1000 \frac{mol}{m^3}$	[49]
Double layer capacitance anode	$C_{DL,a}$	$0.228 \frac{F}{m^2}$	Identified from 0.1Hz to 10kHz impedance measurement at 50 % SOC
Double layer capacitance cathode	$C_{DL,c}$	$0.818 \frac{F}{m^2}$	Identified from 0.1Hz to 10kHz impedance measurement at 50 % SOC
Exchange current rate anode	$i_{00,a}$	$1.47 \times 10^{-14} \frac{Am^{2.5}}{mol^{1.5}}$	Identified from 0.1Hz to 10kHz impedance measurement at 50 % SOC
Exchange current rate cathode	$i_{00,c}$	$0.57 \times 10^{-14} \frac{Am^{2.5}}{mol^{1.5}}$	Identified from 0.1Hz to 10kHz impedance measurement at 50 % SOC
Electric conductivity anode	$\sigma_{s,a}$	$100 \frac{S}{m}$	[3]
Electric conductivity cathode	$\sigma_{s,c}$	$10 \frac{S}{m}$	[50]
transference number	t_+	0.37	[51]
Salt diffusion coefficient	D_e	salt concentration dependent (polynom)	[51]
Charge transfer coefficient anode	α_a	0.463	Adaption to presented NFRA measurements
Charge transfer coefficient cathode	α_c	0.47	Set to a value < 0.5 to detect possible effects of the cathode on Y_2
Plating Parameter			
Reference surface concentration	Γ_{ref}	$1 \times 10^{-5} \frac{mol}{m^2}$	Chosen small while maintaining good numerical stability
Exchange current plating	$i_{00,pl}$	$10 \frac{A}{m^2}$	[3]
Charge transfer coefficient plating	α_{pl}	0.45	Chosen such that $\alpha_a > \alpha_{pl}$ (see Fig. 3 SI)
Areal growth coefficient	k_{pl}	$5 \times 10^3 \frac{m^3}{mol^2}$	Chosen to reproduce additional voltage plateau in relaxation after a 2C charge

Data availability

Research data to reproduce the figures will be shared under the DOI: https://doi.org/10.35097/dvgw05vhcx5qqakt.

References

[1] T. Waldmann, B.I. Hogg, M. Wohlfahrt-Mehrens, Li plating as unwanted side reaction in commercial Li-ion cells – a review, J. Power Sources 384 (2018) 107–124, https://doi.org/10.1016/J.JPOWSOUR.2018.02.063.

[2] U. Janakiraman, T.R. Garrick, M.E. Fortier, Review—lithium plating detection methods in Li-Ion batteries, J. Electrochem. Soc. 167 (2020) 160552, https://doi.org/10.1149/1945-7111/abd3b8.

[3] P. Arora, M. Doyle, R.E. White, Mathematical modeling of the lithium deposition overcharge reaction in lithium-ion batteries using carbon-based negative electrodes, J. Electrochem. Soc. 146 (1999) 3543–3553, https://doi.org/10.1149/1.1392512.

[4] T. Gao, Y. Han, D. Fraggedakis, S. Das, T. Zhou, C.N. Yeh, S. Xu, W.C. Chueh, J. Li, M.Z. Bazant, Interplay of lithium intercalation and plating on a single graphite particle, Joule 5 (2021) 393–414, https://doi.org/10.1016/J.JOULE.2020.12.020.

[5] M. Fleischhammer, T. Waldmann, G. Bisle, B.I. Hogg, M. Wohlfahrt-Mehrens, Interaction of cyclic ageing at high-rate and low temperatures and safety in lithium-ion batteries, J. Power Sources 274 (2015) 432–439, https://doi.org/10.1016/J.JPOWSOUR.2014.08.135.

[6] B. Bitzer, A. Gruhle, A new method for detecting lithium plating by measuring the cell thickness, J. Power Sources 262 (2014) 297–302, https://doi.org/10.1016/J.JPOWSOUR.2014.03.142.

[7] F.B. Spingler, W. Wittmann, J. Sturm, B. Rieger, A. Jossen, Optimum fast charging of lithium-ion pouch cells based on local volume expansion criteria, J. Power Sources 393 (2018) 152–160, https://doi.org/10.1016/J.JPOWSOUR.2018.04.095.

[8] Q.Q. Liu, D.J. Xiong, R. Petibon, C.Y. Du, J.R. Dahn, Gas evolution during unwanted lithium plating in Li-Ion cells with EC-Based or EC-Free electrolytes, J. Electrochem. Soc. 163 (2016) A3010–A3015, https://doi.org/10.1149/2.0711614JES/XML.
[9] J. Arai, Y. Okada, T. Sugiyama, M. Izuka, K. Gotoh, K. Takeda, In situ solid state 7 li NMR observations of lithium metal deposition during overcharge in lithium ion batteries, J. Electrochem. Soc. 162 (2015) A952–A958, https://doi.org/10.1149/2.0411506JES/XML.
[10] H. Ge, T. Aoki, N. Ikeda, S. Suga, T. Isobe, Z. Li, Y. Tabuchi, J. Zhang, Investigating lithium plating in lithium-ion batteries at low temperatures using electrochemical model with NMR assisted parameterization, J. Electrochem. Soc. 164 (2017) A1050–A1060, https://doi.org/10.1149/2.0461706JES/XML.
[11] Y.C. Hsieh, M. Leißing, S. Nowak, B.J. Hwang, M. Winter, G. Brunklaus, Quantification of dead lithium via in situ nuclear magnetic resonance spectroscopy, Cell Rep. Phys. Sci. 1 (2020) 100139, https://doi.org/10.1016/J.XCRP.2020.100139.
[12] C. Bommier, W. Chang, Y. Lu, J. Yeung, G. Davies, R. Mohr, M. Williams, D. Steingart, In operando acoustic detection of lithium metal plating in commercial LiCoO2/Graphite pouch cells, Cell Rep. Phys. Sci. 1 (2020) 100035, https://doi.org/10.1016/J.XCRP.2020.100035.
[13] S. Schindler, M. Bauer, M. Petzl, M.A. Danzer, Voltage relaxation and impedance spectroscopy as in-operando methods for the detection of lithium plating on graphitic anodes in commercial lithium-ion cells, J. Power Sources 304 (2016) 170–180, https://doi.org/10.1016/J.JPOWSOUR.2015.11.044.
[14] M. Bauer, B. Rieger, S. Schindler, P. Keil, M. Wachtler, M.A. Danzer, A. Jossen, Multi-phase formation induced by kinetic limitations in graphite-based lithium-ion cells: analyzing the effects on dilation and voltage response, J. Energy Storage 10 (2017) 1–10, https://doi.org/10.1016/J.EST.2016.11.006.
[15] M. Petzl, M.A. Danzer, Nondestructive detection, characterization, and quantification of lithium plating in commercial lithium-ion batteries, J. Power Sources 254 (2014) 80–87, https://doi.org/10.1016/J.JPOWSOUR.2013.12.060.
[16] M.C. Smart, B.V. Ratnakumar, Effects of electrolyte composition on lithium plating in lithium-ion cells, J. Electrochem. Soc. 158 (2011) A379–A389, https://doi.org/10.1149/1.3544439/XML.
[17] I.D. Campbell, M. Marzook, M. Marinescu, G.J. Offer, How observable is lithium plating? Differential voltage analysis to identify and quantify lithium plating following fast charging of cold lithium-ion batteries, J. Electrochem. Soc. 166 (2019) A725–A739, https://doi.org/10.1149/2.0821904JES/XML.
[18] U.R. Koleti, T.Q. Dinh, J. Marco, A new on-line method for lithium plating detection in lithium-ion batteries, J. Power Sources 451 (2020) 227798, https://doi.org/10.1016/j.jpowsour.2020.227798.
[19] M. Koseoglou, E. Tsioumas, D. Ferentinou, N. Jabbour, D. Papagiannis, C. Mademlis, Lithium plating detection using dynamic electrochemical impedance spectroscopy in lithium-ion batteries, J. Power Sources 512 (2021) 230508, https://doi.org/10.1016/J.JPOWSOUR.2021.230508.
[20] M. Dotoli, E. Milo, M. Giuliano, R. Rocca, C. Nervi, M. Baricco, M. Ercole, M. F. Sgroi, Detection of lithium plating in Li-Ion cell anodes using realistic automotive fast-charge profiles, Batteries 7 (46 7) (2021) 46, https://doi.org/10.3390/BATTERIES7030046, 2021.
[21] F. Katzer, T. Rüther, C. Plank, F. Roth, M.A. Danzer, Analyses of polarisation effects and operando detection of lithium deposition in experimental half- and commercial full-cells, Electrochim. Acta 436 (2022) 141401, https://doi.org/10.1016/J.ELECTACTA.2022.141401.
[22] D.E. Brown, E.J. McShane, Z.M. Konz, K.B. Knudsen, B.D. McCloskey, Detecting onset of lithium plating during fast charging of Li-ion batteries using operando electrochemical impedance spectroscopy, Cell Rep. Phys. Sci. 2 (2021) 100589, https://doi.org/10.1016/J.XCRP.2021.100589.
[23] N. Harting, N. Wolff, U. Krewer, Identification of lithium plating in lithium-ion batteries using nonlinear frequency response analysis (NFRA), Electrochim. Acta 281 (2018) 378–385, https://doi.org/10.1016/j.electacta.2018.05.139.
[24] T. Vidaković-Koch, T. Miličić, L.A. Živković, H.S. Chan, U. Krewer, M. Petkovska, Nonlinear frequency response analysis: a recent review and perspectives, Curr. Opin. Electrochem. 30 (2021) 100851, https://doi.org/10.1016/J.COELEC.2021.100851.
[25] N. Harting, N. Wolff, F. Röder, U. Krewer, Nonlinear frequency response analysis (NFRA) of lithium-ion batteries, Electrochim. Acta 248 (2017) 133–139, https://doi.org/10.1016/j.electacta.2017.04.037.
[26] N. Harting, R. Schenkendorf, N. Wolff, U. Krewer, State-of-Health identification of lithium-ion batteries based on nonlinear frequency response analysis: first steps with machine learning, Appl. Sci. 8 (2018) 821, https://doi.org/10.3390/app8050821.
[27] N. Wolff, N. Harting, M. Heinrich, F. Röder, U. Krewer, Nonlinear frequency response analysis on lithium-ion batteries: a model-based assessment, Electrochim. Acta 260 (2018) 614–622, https://doi.org/10.1016/j.electacta.2017.12.097.
[28] N. Wolff, N. Harting, F. Röder, M. Heinrich, U. Krewer, Understanding nonlinearity in electrochemical systems, Eur. Phys. J.: Spec. Top. 227 (2019) 2617–2640, https://doi.org/10.1140/epjst/e2019-800135-2.
[29] M.D. Murbach, D.T. Schwartz, Extending newman's pseudo-two-dimensional lithium-ion battery impedance simulation approach to include the nonlinear harmonic response, J. Electrochem. Soc. 164 (2017) E3311–E3320, https://doi.org/10.1149/2.0301711jes.
[30] H.S. Chan, Y.Y. Lee, D. Witt, J. Ulrich, A. Weber, U. Krewer, Improved identifiability of kinetic parameters in lithium-ion batteries via nonlinear frequency response analysis, Batter Supercaps (2025) e202500179, https://doi.org/10.1002/BATT.202500179.
[31] N. Wolff, N. Harting, M. Heinrich, U. Krewer, Nonlinear frequency response analysis on lithium-ion batteries: process identification and differences between transient and steady-state behavior, Electrochim. Acta 298 (2019) 788–798, https://doi.org/10.1016/j.electacta.2018.12.107.
[32] M. Doyle, T.F. Fuller, J. Newman, Modeling of galvanostatic charge and discharge of the lithium/polymer/insertion cell, J. Electrochem. Soc. 140 (1993) 1526–1533, https://doi.org/10.1149/1.2221597/XML.
[33] A. Jokar, B. Rajabloo, M. Désilets, M. Lacroix, Review of simplified pseudo-two-dimensional models of lithium-ion batteries, J. Power Sources 327 (2016) 44–55, https://doi.org/10.1016/J.JPOWSOUR.2016.07.036.
[34] U. Krewer, F. Röder, E. Harinath, R.D. Braatz, B. Bedürftig, R. Findeisen, Review—dynamic models of Li-Ion batteries for diagnosis and operation: a review and perspective, J. Electrochem. Soc. 165 (2018) A3656–A3673, https://doi.org/10.1149/2.1061814JES/XML.
[35] K.A. Smith, Electrochemical control of lithium-ion batteries, IEEE Control Syst. 30 (2010) 18–25, https://doi.org/10.1109/MCS.2010.935882.
[36] D.R. Baker, M.W. Verbrugge, Modeling overcharge at graphite electrodes: plating and dissolution of lithium, J. Electrochem. Soc. 167 (2020) 013504, https://doi.org/10.1149/2.0042001jes.
[37] S. Szabó, S. Szabo, Underpotential deposition of metals on foreign metal substrates, Int. Rev. Phys. Chem. 10 (1991) 207–248, https://doi.org/10.1080/01442359109353258.
[38] S. Hein, T. Danner, A. Latz, An electrochemical model of lithium plating and stripping in lithium ion batteries, ACS Appl. Energy Mater. 3 (2020) 8519–8531, https://doi.org/10.1021/acsaem.0c01155.
[39] M.D. Murbach, V.W. Hu, D.T. Schwartz, Nonlinear electrochemical impedance spectroscopy of lithium-ion batteries: experimental approach, analysis, and initial findings, J. Electrochem. Soc. 165 (2018) A2758–A2765, https://doi.org/10.1149/2.0711811jes.
[40] Zahner Elektrik GmbH, Nonlinear frequency response analysis (NFRA). Zahner Device Manual, 2024. https://doc.zahner.de/manuals/nfra.pdf. (Accessed 9 January 2025).
[41] D.D. Weiner, J.F. Spina, Sinusoidal Analysis and Modeling of Weakly Nonlinear Circuits: with Application to Nonlinear Interference Effects, Van Nostrand Reinhold, New York, N.Y., 1980.
[42] D. Witt, F. Röder, U. Krewer, Analysis of Lithium-Ion Battery State and Degradation via Physicochemical Cell and SEI Modeling, Batter Supercaps, 2022, https://doi.org/10.1002/BATT.202200067.
[43] S. Carelli, W.G. Bessler, Prediction of reversible lithium plating with a Pseudo-3D lithium-ion battery model, J. Electrochem. Soc. 167 (2020) 100515, https://doi.org/10.1149/1945-7111/AB95C8.
[44] M.W. Verbrugge, B.J. Koch, Microelectrode investigation of ultrahigh-rate lithium deposition and stripping, J. Electroanal. Chem. 367 (1994) 123–129, https://doi.org/10.1016/0022-0728(93)03047-S.
[45] M. Verbrugge, D. Baker, B. Koch, X. Xiao, W. Gu, Thermodynamic model for substitutional materials: application to lithiated graphite, spinel manganese oxide, iron phosphate, and layered nickel-manganese-cobalt oxide, J. Electrochem. Soc. 164 (2017) E3243–E3253, https://doi.org/10.1149/2.0341708JES/XML.
[46] D.R. Baker, M.W. Verbrugge, Multi-species, multi-reaction model for porous intercalation electrodes: part I. Model formulation and a perturbation solution for low-scan-rate, linear-sweep voltammetry of a spinel lithium manganese oxide electrode, J. Electrochem. Soc. 165 (2018) A3952–A3964, https://doi.org/10.1149/2.0771816JES/XML.
[47] M. Doyle, Y. Fuentes, Computer simulations of a lithium-ion polymer battery and implications for higher capacity next-generation battery designs, J. Electrochem. Soc. 150 (2003) A706, https://doi.org/10.1149/1.1569478/XML.
[48] V. Laue, F. Röder, U. Krewer, Joint structural and electrochemical modeling: impact of porosity on lithium-ion battery performance, Electrochim. Acta 314 (2019) 20–31, https://doi.org/10.1016/J.ELECTACTA.2019.05.005.
[49] M. Guo, G. Sikha, R.E. White, Single-particle model for a lithium-ion cell: thermal behavior, J. Electrochem. Soc. 158 (2011) A122, https://doi.org/10.1149/1.3521314.
[50] J. Schmalstieg, D.U. Sauer, Full cell parameterization of a high-power lithium-ion battery for a physico-chemical model: part II. Thermal parameters and validation, J. Electrochem. Soc. 165 (2018) A3811–A3819, https://doi.org/10.1149/2.0331816JES/XML.
[51] L.O. Valøen, J.N. Reimers, Transport properties of LiPF[sub 6]-Based Li-Ion battery electrolytes, J. Electrochem. Soc. 152 (2005) A882, https://doi.org/10.1149/1.1872737.